HHS Public Access

Author manuscript

Cell Host Microbe. Author manuscript; available in PMC 2017 February 10.

Published in final edited form as:

Cell Host Microbe. 2016 February 10; 19(2): 254–266. doi:10.1016/j.chom.2016.01.002.

Integrated omics analysis of pathogenic host responses during pandemic H1N1 influenza virus infection: the crucial role of lipid metabolism

Jennifer Tisoncik-Go[1,10], **David J. Gasper**[3,10], **Jennifer E. Kyle**[4], **Amie J. Eisfeld**[3], **Christian Selinger**[1], **Masato Hatta**[3], **Juliet Morrison**[1], **Marcus J. Korth**[1], **Erika M. Zink**[4], **Young-Mo Kim**[4], **Athena A. Schepmoes**[4], **Carrie D. Nicora**[4], **Samuel O. Purvine**[5], **Karl K. Weitz**[4], **Xinxia Peng**[1], **Richard R. Green**[1], **Susan C. Tilton**[4], **Bobbie-Jo Webb-Robertson**[6], **Katrina M. Waters**[4], **Thomas O. Metz**[4], **Richard D. Smith**[4], **Yoshihiro Kawaoka**[3,7], **M. Suresh**[3], **Laurence Josset**[2], and **Michael G. Katze**[1]

[1]Department of Microbiology, University of Washington, Seattle, WA, USA

[2]Laboratoire de Virologie, Centre de Biologie Est des Hospices Civils de Lyon, Université Claude Bernard Lyon 1, Lyon, France

[3]Department of Pathobiological Sciences, School of Veterinary Medicine, University of Wisconsin, Madison, WI, USA

[4]Biological Sciences Division, Pacific Northwest National Laboratory, Richland, WA, USA

[5]Environmental Molecular Sciences Laboratory, Pacific Northwest National Laboratory, Richland, WA, USA

[6]Computational and Statistical Analytics Division, Pacific Northwest National Laboratory, Richland, WA, USA

[7]Division of Virology, Department of Microbiology and Immunology, Institute of Medical Science, University of Tokyo, Tokyo 108-8639; Japan Department of Special Pathogens, International Research Center for Infectious Diseases, Institute of Medical Science, University of Tokyo, Minato-ku, Tokyo 108-8639; Japan; Laboratory of Bioresponses Regulation, Department of Biological Responses, Institute for Virus Research, Kyoto University, Kyoto 606-8507, Japan

[8]Washington National Primate Research Center, Seattle, Washington, USA

Contact: Correspondence should be addressed to Michael G. Katze at honey@uw.edu.
Current address: David J. Gasper; Pacific Zoo & Wildlife Diagnostics, San Diego, CA 92130, USA
Current address: Christian Selinger; Institute for Disease Modeling, Bellevue, WA 98004, USA
Current address: Susan C. Tilton; Environmental and Molecular Toxicology; Oregon State University, Corvallis, OR 97331, USA
[10]Co-first authors Jennifer Tisoncik-Go and David J. Gasper

AUTHOR CONTRIBUTIONS

Conceptualization and Methodology Y.K., M.S. and M.G.K.; Supervision, A.J.E., L.J. and T.O.M.; Project Administration, R.D.S., T.O.M., and K.M.W.; Investigation, D.J.G., M.H., J.E.K., E.M.Z., Y-M.K., A.A.S, C.D.N., S.O.P and K.K.W.; Formal Analysis, J.T.-G., L.J., R.G., C.S., X.P., S.C.T., and B-J.W-R.; Writing – Original Draft J.T.-G., D.J.G. and T.O.M.; Writing – Review & Editing, J.T.-G., D.J.G., T.O.M., and M.J.K.; Visualization, J.T.-G., D.J.G., and J.M.; Funding Acquisition, D.J.G., M.G.K. and R.D.S.

SUMMARY

Pandemic influenza viruses modulate pro-inflammatory responses that can lead to immunopathogenesis. We present an extensive and systematic profiling of lipids, metabolites and proteins in respiratory compartments of ferrets infected with either 1918 or 2009 human pandemic H1N1 influenza viruses. Integrative analysis of high-throughput omics data with virologic and histopathologic data uncovered relationships between host responses and phenotypic outcomes of viral infection. Pro-inflammatory lipid precursors in the trachea following 1918 infection correlated with severe tracheal lesions. Using an algorithm to infer cell quantity changes from gene expression data, we found enrichment of distinct T cell subpopulations in the trachea. There was also a predicted increase in inflammatory monocytes in the lung of 1918 virus-infected animals that was sustained throughout infection. This study presents a unique resource to the influenza research community and demonstrates the utility of an integrative systems approach for characterization of lipid metabolism alterations underlying respiratory responses to viruses.

INTRODUCTION

Highly pathogenic influenza viruses cause robust and sustained pro-inflammatory responses that enhance immunopathology in the lung. Significant progress has been made in elucidating innate immune responses contributing to the pathogenesis of these medically important viral pathogens, yet important questions remain. Chief among these is how alterations in the host metabolic state during influenza virus infection impacts respiratory disease severity and progression. The domestic ferret (*Mustela putorius furo*) is highly utilized as a model of influenza pathogenesis and transmission. Ferrets are naturally susceptible to human influenza virus and present clinical symptoms akin to humans. Cellular sialyllactose receptors promoting viral entry are similarly distributed within the respiratory tract between ferrets and humans. This was recently reinforced by the discovery of a deletion in the ferret *CMAH* gene resulting in the exclusive expression of *N*-acetylneuramininic acid (Neu5Ac) on cell surfaces, as seen with humans (Ng et al., 2014).

With the sequencing of the ferret genome (Peng et al., 2014), it is now possible to perform systems-level analyses. We previously evaluated the global transcriptional response induced in the trachea and lung of ferrets infected with either 1918 or 2009 human pandemic H1N1 influenza viruses and found an enrichment of genes associated with lipid receptor signaling in the trachea (Peng et al., 2014). Lipids are important modulators of inflammation and their role in influenza virus infection is the subject of increasing investigation. Tam et al. recently found that the ratio of specific pro-inflammatory and anti-inflammatory lipids may be markers of influenza virus pathogenicity in mice (Tam et al., 2013). In a separate study, treatment of ferrets with an agonist of sphingosine-1-phosphate (S1P) 1 receptor was found to suppress cytokine and chemokine production during pandemic influenza H1N1 virus infection (Teijaro et al., 2014). These studies indicate a role for lipid signaling pathways in the regulation of inflammation during influenza virus infection. Moreover, lipids and the pathways that they regulate may provide a therapeutic strategy for ameliorating disease by dampening inflammatory responses attending viral infection.

Here, we present a systematic profiling of lipids, metabolites and proteins in upper and lower respiratory compartments of ferrets infected with either 1918 or 2009 human pandemic H1N1 influenza viruses. Through an integrative network analysis we identified relationships between groups of different molecular species in the host response during influenza virus infection. We also examined relationships in independent virus and tissue networks that were correlated with viral replication and respiratory disease. We found groups of lipids and metabolites positively correlated with genes enriched for cell differentiation and adhesion processes. We also found enrichment of T cell genes late in infection that was enhanced in the trachea compared to the lung and corroborated using Digital Cell Quantifier (DCQ), a computational method to infer distinct immune cell subpopulations. Correlation analysis found tissue damage was associated with phospholipids containing arachidonic acid (20:4) and DHA (22:6) that may act as reservoirs for lipid mediators regulating inflammatory responses to pandemic H1N1 influenza virus infection.

RESULTS

Lipidomic and metabolomic analysis of lung and trachea from ferrets infected with pandemic H1N1 influenza viruses

Ferrets were inoculated intranasally with either influenza A/California/04/2009 (CA04) virus or influenza A/Brevig Mission/1/1918 (1918) virus. On days 1, 3 and 8 post-inoculation (p.i.), lung and trachea samples were collected to analyze lipids by LC-MS/MS and metabolites by GC-MS. We identified 488 unique lipids in the lung and 191 in the trachea. Fifteen different lipid subclasses were represented, with triacylglycerol (TG) and diacylglycerophosphocholine (PC) subclasses having the greatest relative abundances in the two tissues (Figure 1A and 1B). There was a larger relative percentage of diacylglycerophosphoglycerol (PG) in the lung compared to the trachea. We also identified 91 metabolites in the lung and 86 metabolites in the trachea. Overall, there was a greater number of differentially abundant (DA) metabolites with decreased abundance in the two tissues for 1918 and CA04 infections (Figure 1C) that included essential amino acids.

We next inferred a co-expression network based on log2FC abundances for 50 DA lipids and 33 DA metabolites. The network was composed of nodes, corresponding to lipids and metabolites, and edges between nodes that show co-abundance patterns for 1918 and CA04 infections in the two tissues. The nodes were organized into modules arbitrarily assigned numbers (1 to 19) concatenated with the prefix “lm”. The modules represent groups of coexpressed molecular species that often share similar biological functions. There were modules that exhibited tissue-specific patterns in lipid and metabolite abundance profiles, such as module lm18 containing ethanolamine, glyceric acid, and uracil (Figure 1D and Table S1). These metabolites showed increased abundance in the trachea compared to the lung and were co-expressed with sphingomyelin specie, SM(d18:1/24:1), and PC(0:0/18:1) and PC(0:0/16:0) lipid species. Within this same module, referred to as the ‘sphingomyelin module’, were two unknown metabolites that may be functionally related to the trachea metabolic response to influenza virus infection. This network analysis identified groups of co-expressed lipids and metabolites, known and unknown, capturing the dynamic changes in

the ferret lipidome and metabolome during pandemic H1N1 influenza virus infection in ferrets.

Histological differences in severity, distribution, and progression of lung and tracheal lesions in CA04- versus 1918-infected ferrets

To determine tissue-level responses, we performed a histopathologic assessment of paired tissue sections from each ferret. No significant histologic findings were observed in the lung on day 1 p.i. At day 3 p.i., multifocal submucosal gland necrosis was the most prominent and consistent lesion in both the 1918 (Figures 2A and 2C) and CA04 groups (Figures 2B and 2D). Compared to the 1918 group (Figure 2E), a severe bronchiolitis was present in the CA04 group only (Figure 2F), with necrotic debris, macrophages, eosinophils, and neutrophils obstructing the airways (see the inset in Figure 2F). Acute alveolar damage and effusion were widespread in the peripheral lungs of 1918-infected animals and generally not associated with airways (Figure 2G). In CA04-infected animals, alveolar damage tended to localize around affected bronchioles, which were lined by variably hypertrophic and hyperplastic type-II pneumocytes (see the left inset in Figure 2H). Foamy macrophages were common in regions of effusion in the CA04 group (see the right inset in Figure 2H), while neutrophils were frequent in lung infected with 1918. At day 8 p.i., the bronchiolitis observed with CA04 infection was largely replaced by mixed mesenchymal and epithelial proliferations (Figure S1). These proliferations partially obstructed bronchioles (bronchiolitis obliterans) and widely extended into the adjacent parenchyma (organizing pneumonia), and have been previously reported (Memoli et al., 2011). Though less severe compared to CA04 infection, bronchiolitis in 1918-infected animals was accompanied by neutrophilic and eosinophilic infiltrates in areas with concurrent glandular necrosis.

In tracheal sections from mock-infected ferrets, there were infrequent intraepithelial lymphocytes in most sections, and sporadic individual or small clusters of intraepithelial eosinophils (Figure 3A). At day 1 p.i., there was extensive inflammatory infiltrate that was accompanied by epithelial changes in 1918-infected trachea (Figure 3B), whereas CA04 infection resulted in mildly increased submucosal lymphocytic infiltrate (Figure 3C). Two of 3 ferrets in the 1918 group exhibited multiple dense nodular aggregates of eosinophils that locally expanded and disrupted the epithelium (see the inset in Figure 3B). The most prominent change from day 1 to day 3 p.i. was multifocal necrosis of the tracheal submucosal glands with glandular and periglandular infiltration of eosinophils, neutrophils, histiocytes, and lymphocytes. Necrosis was most prominent in 1918 virus-infected animals, in which 40% (12 of 30 lobules) of the glands were affected (Figure 3D). In contrast, only 9% (5 of 38 lobules) of the glands were affected following CA04 infection (Figure 3E). Viral antigens were mainly detected in the epithelial cells of submucosal glands (see insets in Figure 3D and 3E). By day 8 p.i., submucosal glandular lesions extended to 75% (24 of 32) of the lobules in the 1918 group (Figure 3F) and 41% (18 of 44) of the lobules in the CA04 group (Figure 3G). Moderately dense aggregates of lymphocytes infiltrated the epithelium in the areas overlying affected glands. In summary, 1918 and CA04 infections differed in the severity and progression of histologic lesions in the lung and trachea, with ferrets infected with CA04 virus presenting more severe bronchiolitis compared to the enhanced tracheitis and tracheoadenitis resulting from 1918 infection.

Metabolic changes correlate with viral replication and disease phenotypes

Relationships between lipid metabolite network modules and virologic (Table S2) and histopathologic phenotypes (File S1) were assessed to identify lipid metabolism changes correlated with viral replication and disease. Both viruses replicated in the trachea on days 1 and 3 p.i. and while 1918 replicated in the lung on days 1 and 3 p.i., CA04 was only recovered on day 3 p.i. from ferret #295 that displayed the most striking necrotizing bronchiolitis. No infectious viruses were recovered from either tissue on day 8 p.i. We found the sphingomyelin module (lm18) was positively correlated with both viral titer and viral mRNA, while module lm14 containing L-threonine and L-valine was strongly anti-correlated with viral titer ($r = -0.75$, p-val<1e-05) (Figure 4A). Several modules were correlated with histopathologic changes in the tissues. Modules lm1, lm8 and lm15 were positively correlated with bronchitis/iolitis, bronchoadenitis, and alveolitis. Module lm8 was also highly correlated with tracheoadenitis ($r = 0.83$, p-val<4e-06), while lm13 and lm17 were negatively correlated with tracheitis. The ‘disease’ modules consisted mostly of diacylglycerophosphoethanolamine (PE), PE(P–, and PC lipid species containing either 22:6 or 20:4, the precursor of docosahexaenoic acid (DHA) and arachidonic acid (AA), respectively (Table S1). In particular, we found PC(18:1/20:4) and PC(16:0/22:6) species from lm1 had earlier increased abundance in both the lung and trachea in response to 1918 virus compared to CA04 virus (Figure 1D). Multinomial ordered logistic regression analysis of histologic lesions scores found a more significant contribution by 1918 toward disease severity in the trachea relative to CA04 (odds ratio of 0.352) (Table S3). Thus, an increase in pro-inflammatory lipids in the trachea may be enhancing necrosis and inflammation associated with 1918 influenza virus infection.

We complemented the lipidomic and metabolomics analysis by assessing the proteome in paired tissue sections. LC/MS analysis identified 4,811 proteins in the lung and 4,060 proteins in the trachea. We then inferred a co-expression network based on log2FC abundances for 810 DA proteins and identified tissue-specific protein profiles in response to influenza virus infection (Figure 4B); these differences were also visualized by multidimensional scaling (Figure 4C). In addition, a gene co-expression network was constructed using a transcriptional signature enriched with putative intergenic non-coding RNAs that was derived from a tissue-by-virus comparison of ferret RNA-Seq data (Peng et al., 2014) (Figure S2A and S2B). Modules were arbitrarily assigned numbers concatenated with prefixes “p” and “g” for protein and gene networks, respectively. The protein network was enriched for hematological system development and function, glycolysis, and cellular oxidative stress processes (Table S4). We also found proteins related to innate immune and antiviral responses including Trim25, Stat1, Mx1, as well as p120-catenin (encoded by *CTNND1* gene) known to protect alveolar epithelial barrier integrity (Chignalia et al., 2015). In relation to lipid metabolism, protein module p2 contained apolipoproteins, Apoh and Apoa4, and gene module g5 contained fatty acid metabolism genes, *FABP3* and *SCD*, as well as *PTGER3*, encoding a receptor of PGE_2 known to inhibit alveolar macrophage type I interferon responses during influenza virus infection (Coulombe et al., 2014) (Table S5). This comprehensive analysis implicates a shift toward increased lipid metabolism that may be integral in antiviral responses toward pandemic H1N1 influenza virus infection.

Integrated omics analysis shows temporal and regional dynamics of the host response to pandemic H1N1 influenza virus infection

To examine relationships between lipids, metabolites, proteins and genes in toto, we constructed an integrated omics network by calculating the pairwise correlations between module eigengenes (MEs)—the representative expression profile of each module characterized by its first principal component—from each independent network and between MEs and phenotypic traits (Figure S3). A primary goal of this integrative analysis was to characterize host responses in a unified model of influenza pathogenesis, as well as previously unidentified molecular species associated with known innate and adaptive immune responses important in the control of viral infection. Gene modules g2 and g10, which were enriched for host defense genes relevant to influenza virus infection, strongly correlated with viral titer and mRNA (Figure 5A and Figure S2D). There was positive correlation of the sphingomyelin module (lm18) with these innate immune gene modules, and by association the lipid metabolism p2 module, suggesting these lipids and lipid-related proteins are involved in innate immune responses controlling influenza virus replication. In examining module relationships with disease phenotypes, we found positive correlations between tracheitis, tracheoadenitis, and bronchitis/iolitis with gene module g3, enriched for T cell genes, and g6 enriched for genes associated with calcium signaling (Figure 5B and Figure S2C). In particular, module g6 contained *ATP2B4, CAMK2G*, and *CAMKK1* genes, as well as *ORAI1*, transcribing a subunit of the calcium-release-activated calcium (CRAC) channel known to regulate intracellular Ca2+ concentrations essential for the activation of cytokine gene expression in T cells.

The richness of the datasets comprising the integrated network is further exemplified by the presence of relationships between modules of different molecular species (e.g., lipid metabolites and genes, proteins and genes, and lipid metabolites and proteins) (Figure 5C). In comparing the two tissues, the dynamics of the host response were largely different; the trachea showed greater variability in changes in gene expression and lipid, metabolite and protein abundance during 1918 and CA04 infections compared to the lung responses that were more consistent across time-points and viruses (Figure 5D). Taken together, this integrative analysis demonstrates highly interrelated relationships among diverse molecular species of the host response that regulate the progression and severity of respiratory disease associated with pandemic H1N1 influenza virus infection and control viral replication.

Increased lymphocyte responses in the trachea at later stages of infection is associated with inflammation

The interrelationships of this complex integrated network were computationally elucidated by recalculating the ME for each module of the integrated network considering trachea, lung, 1918 and CA04 samples independently, and then computing pairwise bicor between MEs within the four separate networks. Here, we show examples of relationships that are conserved between tissues and viruses (abs Δbicor<0.7) and report previously unidentified molecular species likely playing a role in the immune response against influenza virus. In the lung and trachea networks, we found several similarly correlated relationships, such as the relationship between the innate immune g4 module and viral titer (abs Δbicor = −0.08), indicating comparable innate immune responses represented in the two tissues that are

correlated with viral replication (File S3). There were also several relationships with apparent differences (abs Δbicor>0.7) between tissues, such as g10:lm12 and p2:p4 (Figure 6A and 6B), suggesting cellular processes involving lipids, genes and proteins specific to a particular respiratory compartment. For example, the g1:g7 relationship was positively correlated in the lung (bicor = 0.71) and anticorrelated in the trachea (bicor = −0.67) (Figure 6A). The g7 module is enriched for downregulated genes related to signal transduction and neurological stimuli responses, including the *NPY2R* gene encoding neuropeptide Y2 receptor known to play a critical role in allergic airway inflammation. This relationship may signify neurologic peptide responses modulating influenza virus infection in the lung and independent of the trachea.

Another example of a host response relationship largely different between the two tissues is the g13:g3 relationship, which shows a strong positive correlation in the trachea (bicor = 0.81) that is opposite from the lung (bicor = −0.51) (Figure 6B). Topological analysis of module g3, enriched for genes associated with T cell receptor signaling, identified several intergenic transcripts as intramodular hubs (Figure 6C). These central nodes and their highly connected nodes representing lymphocyte genes had increased expression in the trachea at day 8 p.i. in response to both 1918 and CA04 infections (Figure 6D). To further explore these findings, we analyzed the transcriptomic data using Digital Cell Quantifier (DCQ) to predict relative immune cell quantities in the trachea. This computational method combines genome-wide gene expression data with a mouse immune cell compendium that has been used to infer changes in distinct dendritic cell (DC) subpopulations in mouse lung infected with influenza virus (Altboum et al., 2014). In ferrets, we found influenza virus infection elicited temporal differences in specific T cell subpopulations and resident monocytes that were most apparent at day 8 p.i. (Figure 6E). In particular, there were predicted increases in CD8+ memory and effector T cells and Ly6C- ‘resident’ monocyte subtypes (MO.Ly6C^{-}MHCII^{-} and MO.Ly6C^{-}MHCII^{INT}) (Table S6). There was also a DC population (CD11c^{+}MHCII^{hi}CD103^{-}CD11b^{+}) that was initially larger in ferrets infected with 1918 virus that progressively declined by day 8 p.i. Thus, investigation of network variation uncovered putative intergenic non-coding RNAs induced late in infection that may be central to the resolution of viral infection by regulating lymphocyte responses in upper respiratory tissues where human H1N1 influenza viruses predominantly replicate.

In the 1918 and CA04 networks, we found several conserved (abs Δbicor<0.7) relationships, such as the g10:lm13 relationship (bicor = −0.05), with g10 enriched for genes associated with IFN-β and TNF cellular defense responses and lm13 containing palmitic acid and unknown metabolites (File S4). Several relationships had marked differences (abs Δbicor>0.7) between viruses, including g8:g9 and g18:lm3 (Figure 7A and 7B), suggesting these relationships may be specific to either CA04 or 1918 infections. For example, lm3 was positively correlated with g18 for the 1918 group, and it was negatively correlated with 1918 virus-associated alveolitis (bicor = −0.80) (Figure 7B). The lm3 module was enriched for TGs with decreased abundance in the lung and to a greater extent for 1918 compared to CA04, particularly at day 8 p.i. (Figure 7C). Application of DCQ to the lung transcriptomic data showed the presence of Ly6C+ ‘inflammatory’ monocytes for both 1918 and CA04 infections (Figure 7D). Notably, there was one monocyte subpopulation (MO.6C+II−.BM) that was enriched specifically in ferret lung infected with 1918 virus throughout infection.

1918 virus is known to cause massive recruitment of monocytes into mouse lung (Perrone et al., 2008). These analyses indicate pathogenic processes in CA04 and 1918 infections are mediated in a particular context (i.e., respiratory compartment and lipid specie) or by the presence of specific immune cells that can depend on the viral strain.

DISCUSSION

We took advantage of the recent sequencing of the ferret genome to study host responses correlated with the pathogenesis of pandemic influenza virus. Through an integrative network analysis we examined relationships among different molecular species in the trachea and lung of ferrets infected with either 1918 or CA04 viruses. We found significant abundance changes for phospholipids (PC and PE species) that are major constituents of pulmonary surfactant known to suppress influenza infection in bronchial epithelial cells (Numata et al., 2012). In addition, several phospholipids contained 20:4 that can be cleaved to form arachidonic acid, the precursor to eicosanoids converted by cyclooxygenase-2 (COX-2), including prostaglandins (e.g., PGE_2 and PGI_2) and leukotrienes (e.g., LTB_4). In particular, PC(18:1/20:4) and PE(18:0/22:4) species were correlated with histologic lesions in the lung and trachea and had increased abundance that was greater in response to 1918 compared to CA04. Thus, tissue damage during pandemic H1N1 influenza virus infection may be the result of lipid mediators derived from phospholipid arachidonic acid (20:4) reservoirs that serve to enhance inflammatory responses.

In a mouse model, arachidonic acid has been implicated in the pathogenesis of avian H5N1 influenza virus (Morita et al., 2013). High viral load and excessive inflammation caused by hypercytokinemia (referred to as a cytokine storm) contribute to H5N1 pathogenesis and a fatal outcome in humans (de Jong et al., 2006; Tisoncik et al., 2012). Lung tissue from patients with fatal outcomes of H5N1 infection shows extensive COX-2 induction in epithelial cells that mediates a pro-inflammatory cascade resulting in increased chemotaxis and vascular permeability (Lee et al., 2008). Therefore, an effective therapy may be one that targets both the virus and pro-inflammatory responses contributing to disease severity through the combination of antivirals and immunomodulatory agents. This was demonstrated using a combination therapy consisting of the anti-influenza neuraminidase inhibitor, zanamivir, together with the anti-inflammatory COX-2 inhibitors celecoxib and mesalazine, which increased survival rate of mice infected with H5N1 virus (Zheng et al., 2008). In targeting the COX pathway, proinflammatory cytokines and eicosanoids can be alleviated, thereby decreasing the activation of inflammatory macrophages and neutrophils.

We previously reported that the presence of foamy macrophages in CA04 virus-infected airways is associated with nuclear activation of heterodimer liver X receptor (LXR) and retinoic acid receptor (RXR) leading to altered lipid metabolism (Go et al., 2012). In the current study, foamy macrophages were found in regions of effusion following infection with CA04 but not 1918. Foams cells are known to accumulate triacyglycerols (TGs) that are stored in cytosolic lipid droplets observed with mycobacterium tuberculosis infection (Mehrotra et al., 2014). The TG abundance changes in ferrets infected with pandemic influenza virus correlated with respiratory disease and may signify metabolic fluctuations leading to formation of foamy macrophages as a pathogenic mechanism of CA04 infection.

Thus, the lipidomic alterations in response to pandemic H1N1 influenza virus infection partially reflect the differential distribution and presumed etiopathogenesis of the alveolar effusion and associated histologic lesions in ferrets. It also suggests that the role of lipid signaling pathways in the inflammatory response varies by site and types of insult.

To identify potential cellular sources of immunopathogenesis, we applied the Digital Cell Quantifier (DCQ) algorithm that infers changes in cell quantities from gene expression data obtained from a complex tissue. There was evidence of a DC subpopulation in the trachea early in infection that was followed by the emergence of a prominent population of CD8 T cells with effector and memory phenotypes at day 8 p.i., possibly suggesting initial DCs playing a proinflammatory role by producing cytokines, such as IL-12, IL-23 and TNF, that drive differentiation of IFN-γ-producing T cells at a later stage. This may also contribute to more rapid viral clearance in the trachea of CA04-infected animals that is supported by fewer lesions in CA04-infected trachea and increased glandular necrosis in the 1918-infected trachea. In the lung, there was a virus-specific differential immune cell population, though most enriched cell types did not change between 1918 and CA04 over the course of the infection. The notable difference was a certain monocytic cell type (MO.Ly6C+MHCII-) in the 1918 group compared to the CA04 group. In mice, Ly6C+ monocytes are preferentially recruited into inflamed tissue through their interaction with chemokine receptor CCR2 (Audoy-Remus et al., 2008) and mature to inflammatory macrophages, which secrete TNF and type I IFN in response to viral ligands (Barbalat et al., 2009), contributing to tissue degradation and T cell activation. Targeting inflammatory monocytes by siRNA-mediated silencing of CCR2 attenuates inflammatory disease in mouse models of atherosclerosis and myocardial infarction (Leuschner et al., 2011). These innate immune cells may play a role in enhancing the immunopathology of 1918 infection in the lung of ferrets and thus, potentially serve as therapeutic targets to alleviate inflammation associated with pandemic influenza virus infection.

The extensive amount of high-throughput data generated by this study are of value to the scientific community, particularly to those interested in extracting information about innate immune responses during acute viral infection. For example, the TRIM superfamily has many IFN-inducible members, some known to regulate viral RNA sensing pathways, such as TRIM25-mediated activation of RIG-I (Gack et al., 2009), and others known to function as host restriction factors. Most TRIM members have yet to be described. Within the integrated network, there are 31 TRIM genes primarily grouped into modules enriched for genes associated with innate immune responses (TRIM25 was found in g2). Considering that these groups of co-expressed molecular species often share similar biological functions; the network can be mined to elucidate potential functions of previously uncharacterized TRIM members during influenza virus infection. In summary, respiratory responses to pandemic H1N1 influenza virus infection encompass highly interrelated cellular processes regulating inflammation, cellular immunity, and tissue repair and regeneration. By examining these processes and their relationships in an integrative network analysis, we have captured dynamic changes of important lipids involved in inflammatory processes associated with influenza virus infection.

EXPERIMENTAL PROCEDURES

Lipidomics, metabolomics, and proteomics analyses

Sample extracts from dissected lung and trachea tissues ($n = 42$) were prepared for global lipidomics, metabolomics, and proteomics analyses. Lipid extracts were analyzed by liquid chromatography tandem mass spectrometry (LC-MS/MS) in both positive and negative ionization using HCD (higher-energy collision dissociation) and CID (collision-induced dissociation). Metabolite extracts were analyzed by gas chromatography–mass spectrometry (GC-MS), and protein extracts were analyzed by LC-MS analysis. Datasets were processed in a series of steps using MatLab® R2013b that included filtering lipids, metabolites and peptides with inadequate information, sample outlier detection, and normalization. Proteomics .raw files are available at MassIVE corresponding to accession number MSV000079114. Metabolite and lipid .raw files are available at MetaboLights corresponding to Study Identifier MTBLS196. Ferret RNA-Seq data derived from the same infected ferrets was previously reported (Peng et al., 2014) and are publicly available in the NCBI Short Read Archive (SRA) corresponding to BioProject PRJNA78317 and SRA accession SRX389385.

Integrative network analysis of ferret respiratory responses

Signed weighted coexpression networks were constructed using 50 differentially abundant (DA) lipids and 33 DA metabolites, 810 DA proteins, and 12,918 differentially expressed (DE) genes after exclusion of entries with more than 50% missing values. Pairwise correlations between all pairs of molecular species using log2FC values was calculated based on the biweight midcorrelation (bicor) method (Langfelder and Horvath, 2012). Molecular species with highly similar co-expression relationships were clustered into modules arbitrarily assigned numbers concatenated with prefixes “lm”, “p”, and “g” for the respective lipid metabolite, protein and gene networks. The representative expression profile of each module is characterized by its first principal component (referred to as module eigengene, ME). Pairwise bicor (using maxPOutliers = 0.02) were calculated between MEs representative of all lipid metabolite, protein, and gene modules from the independent networks. Significant correlations between MEs and between MEs and phenotypic data (p-value < 0.05) were visualized in a network using the igraph R package. To evaluate variation in the relationships of the integrated network, we recalculated four different conditions separately: 1) using CA04 (and PBS) samples, 2) 1918 (and PBS) samples, 3) trachea samples and 4) lung samples. Pairwise correlation between ME within each network were calculated using bicor and the difference in coefficients were calculated as $\Delta\text{bicor}_{\text{site}} = \text{bicor}_{\text{lung}} - \text{bicor}_{\text{trachea}}$ and $\Delta\text{bicor}_{\text{virus}} = \text{bicor}_{1918} - \text{bicor}_{\text{CA04}}$.

Pathologic examination

At necropsy, representative tissues were collected from the same lung lobe or 1.5 cm long tracheal segment in each ferret, and preserved by immersion in 10% phosphate-buffered formalin. Following fixation, transverse serial sectioning of each sample at 1.5 to 2 mm intervals yielded 5–8 subsections per tissue. These subsections were then paraffin-embedded and processed for routine histopathology. At least two replicates of 5-μ–thick sections stained with standard hematoxylin and eosin were examined by light microscopy per tissue.

For virus antigen immunohistochemical (IHC) analysis, sections were stained with an inhouse rabbit anti-influenza virus polyclonal antibody (R309) raised against influenza A/WSN/1933 (H1N1) virus (Watanabe et al., 2009). Blinded scoring of histologic lesions in lung and tracheal tissues was performed using an ordinal scale from 0–3, with 0 indicating no lesion, and numbers 1–3 indicating the presence of a lesion and its severity and extent; 1 = mild, 2 = moderate, 3 = severe. For lung sections, separate scoring was performed for three anatomic divisions: 1) large airways (bronchi and bronchioles), 2) terminal airways and alveoli, and 3) submucosal glands. Within each division, separate scores were assigned for the degree of epithelial degeneration, necrosis, regeneration, inflammatory cell infiltration, exudates or effusion, and perivascular lymphocytic cuffing or nodule formation. Tracheal tissues were sectioned transversely, divided into quadrants for scoring, and scored using the same grading system as bronchi and bronchioles, with submucosal glands scored independently. The number and severity of lung tissues per section or tracheal lesions per quadrant were compared between groups. Regionally extensive tracheal cartilage mineralization was present in some cases, and decalcified replicate slides were created by subjecting the original faced-in paraffin blocks to surface decalcification for 10 minutes in Surgipath Decalcifier II (Leica Biosystems) prior to microtomy. A moderate decrease in the staining intensity of cytoplasmic granules in eosinophils was observed in some decalcified replicates.

Supplementary Material

Refer to Web version on PubMed Central for supplementary material.

Acknowledgments

This project has been funded in whole or in part with Federal funds from the National Institute of Allergy and Infectious Diseases, National Institutes of Health, Department of Health and Human Services, under CEIRS Contract No. HHSN272201400006C and Contract No. HHSN272201400005C. Additional support was provided by Public Health Service grants P51OD010425 and U19AI109761 from the National Institutes of Health. David J. Gasper was supported by NIH training grant 5T32OD010423-07 and through The American Association of Immunologists Careers in Immunology Fellowship Program. The proteomics, metabolomics and lipidomics measurements were conducted using capabilities developed under NIGMS Grant P41 GM103493, and the DOE supported Pan-omics Program, and were performed in the Environmental Molecular Science Laboratory, a U.S. Department of Energy (DOE) national scientific user facility at Pacific Northwest National Laboratory (PNNL) in Richland, WA. PNNL is a multi-program national laboratory operated by Battelle for the DOE under Contract DE-AC05-76RLO 1830.

REFERENCES

1. Altboum Z, Steuerman Y, David E, Barnett-Itzhaki Z, Valadarsky L, Keren-Shaul H, Meningher T, Mendelson E, Mandelboim M, Gat-Viks I, et al. Digital cell quantification identifies global immune cell dynamics during influenza infection. Mol Syst Biol. 2014; 10:720. [PubMed: 24586061]
2. Audoy-Remus J, Richard JF, Soulet D, Zhou H, Kubes P, Vallieres L. Rod-Shaped monocytes patrol the brain vasculature and give rise to perivascular macrophages under the influence of proinflammatory cytokines and angiopoietin-2. J Neurosci. 2008; 28:10187–10199. [PubMed: 18842879]
3. Barbalat R, Lau L, Locksley RM, Barton GM. Toll-like receptor 2 on inflammatory monocytes induces type I interferon in response to viral but not bacterial ligands. Nat Immunol. 2009; 10:1200–1207. [PubMed: 19801985]

4. Chignalia AZ, Vogel SM, Reynolds AB, Mehta D, Dull RO, Minshall RD, Malik AB, Liu Y. p120-catenin expressed in alveolar type II cells is essential for the regulation of lung innate immune response. Am J Pathol. 2015; 185:1251–1263. [PubMed: 25773174]
5. Coulombe F, Jaworska J, Verway M, Tzelepis F, Massoud A, Gillard J, Wong G, Kobinger G, Xing Z, Couture C, et al. Targeted prostaglandin E2 inhibition enhances antiviral immunity through induction of type I interferon and apoptosis in macrophages. Immunity. 2014; 40:554–568. [PubMed: 24726877]
6. de Jong MD, Simmons CP, Thanh TT, Hien VM, Smith GJ, Chau TN, Hoang DM, Chau NV, Khanh TH, Dong VC, et al. Fatal outcome of human influenza A (H5N1) is associated with high viral load and hypercytokinemia. Nat Med. 2006; 12:1203–1207. [PubMed: 16964257]
7. Gack MU, Albrecht RA, Urano T, Inn KS, Huang IC, Carnero E, Farzan M, Inoue S, Jung JU, Garcia-Sastre A. Influenza A virus NS1 targets the ubiquitin ligase TRIM25 to evade recognition by the host viral RNA sensor RIG-I. Cell Host Microbe. 2009; 5:439–449. [PubMed: 19454348]
8. Go JT, Belisle SE, Tchitchek N, Tumpey TM, Ma W, Richt JA, Safronetz D, Feldmann H, Katze MG. 2009 pandemic H1N1 influenza virus elicits similar clinical course but differential host transcriptional response in mouse, macaque, and swine infection models. BMC Genomics. 2012; 13:627. [PubMed: 23153050]
9. Langfelder P, Horvath S. Fast R Functions for Robust Correlations and Hierarchical Clustering. J Stat Softw. 2012; 46
10. Lee SM, Cheung CY, Nicholls JM, Hui KP, Leung CY, Uiprasertkul M, Tipoe GL, Lau YL, Poon LL, Ip NY, et al. Hyperinduction of cyclooxygenase-2-mediated proinflammatory cascade: a mechanism for the pathogenesis of avian influenza H5N1 infection. J Infect Dis. 2008; 198:525–535. [PubMed: 18613795]
11. Leuschner F, Dutta P, Gorbatov R, Novobrantseva TI, Donahoe JS, Courties G, Lee KM, Kim JI, Markmann JF, Marinelli B, et al. Therapeutic siRNA silencing in inflammatory monocytes in mice. Nat Biotechnol. 2011; 29:1005–1010. [PubMed: 21983520]
12. Mehrotra P, Jamwal SV, Saquib N, Sinha N, Siddiqui Z, Manivel V, Chatterjee S, Rao KV. Pathogenicity of Mycobacterium tuberculosis is expressed by regulating metabolic thresholds of the host macrophage. PLoS Pathog. 2014; 10:e1004265. [PubMed: 25058590]
13. Memoli MJ, Davis AS, Proudfoot K, Chertow DS, Hrabal RJ, Bristol T, Taubenberger JK. Multidrug-resistant 2009 pandemic influenza A(H1N1) viruses maintain fitness and transmissibility in ferrets. J Infect Dis. 2011; 203:348–357. [PubMed: 21208927]
14. Morita M, Kuba K, Ichikawa A, Nakayama M, Katahira J, Iwamoto R, Watanebe T, Sakabe S, Daidoji T, Nakamura S, et al. The lipid mediator protectin D1 inhibits influenza virus replication and improves severe influenza. Cell. 2013; 153:112–125. [PubMed: 23477864]
15. Ng PS, Bohm R, Hartley-Tassell LE, Steen JA, Wang H, Lukowski SW, Hawthorne PL, Trezise AE, Coloe PJ, Grimmond SM, et al. Ferrets exclusively synthesize Neu5Ac and express naturally humanized influenza A virus receptors. Nat Commun. 2014; 5:5750. [PubMed: 25517696]
16. Numata M, Kandasamy P, Nagashima Y, Posey J, Hartshorn K, Woodland D, Voelker DR. Phosphatidylglycerol suppresses influenza A virus infection. Am J Respir Cell Mol Biol. 2012; 46:479–487. [PubMed: 22052877]
17. Peng X, Alfoldi J, Gori K, Eisfeld AJ, Tyler SR, Tisoncik-Go J, Brawand D, Law GL, Skunca N, Hatta M, et al. The draft genome sequence of the ferret (Mustela putorius furo) facilitates study of human respiratory disease. Nat Biotechnol. 2014; 32:1250–1255. [PubMed: 25402615]
18. Perrone LA, Plowden JK, Garcia-Sastre A, Katz JM, Tumpey TM. H5N1 and 1918 pandemic influenza virus infection results in early and excessive infiltration of macrophages and neutrophils in the lungs of mice. PLoS Pathog. 2008; 4:e1000115. [PubMed: 18670648]
19. Tam VC, Quehenberger O, Oshansky CM, Suen R, Armando AM, Treuting PM, Thomas PG, Dennis EA, Aderem A. Lipidomic profiling of influenza infection identifies mediators that induce and resolve inflammation. Cell. 2013; 154:213–227. [PubMed: 23827684]
20. Teijaro JR, Walsh KB, Long JP, Tordoff KP, Stark GV, Eisfeld AJ, Kawaoka Y, Rosen H, Oldstone MB. Protection of ferrets from pulmonary injury due to H1N1 2009 influenza virus infection: immunopathology tractable by sphingosine-1-phosphate 1 receptor agonist therapy. Virology. 2014; 452–453:152–157.

21. Tisoncik JR, Korth MJ, Simmons CP, Farrar J, Martin TR, Katze MG. Into the eye of the cytokine storm. Microbiol Mol Biol Rev. 2012; 76:16–32. [PubMed: 22390970]

22. Watanabe T, Watanabe S, Shinya K, Kim JH, Hatta M, Kawaoka Y. Viral RNA polymerase complex promotes optimal growth of 1918 virus in the lower respiratory tract of ferrets. Proc Natl Acad Sci U S A. 2009; 106:588–592. [PubMed: 19114663]

23. Zheng BJ, Chan KW, Lin YP, Zhao GY, Chan C, Zhang HJ, Chen HL, Wong SS, Lau SK, Woo PC, et al. Delayed antiviral plus immunomodulator treatment still reduces mortality in mice infected by high inoculum of influenza A/H5N1 virus. Proc Natl Acad Sci U S A. 2008; 105:8091–8096. [PubMed: 18523003]

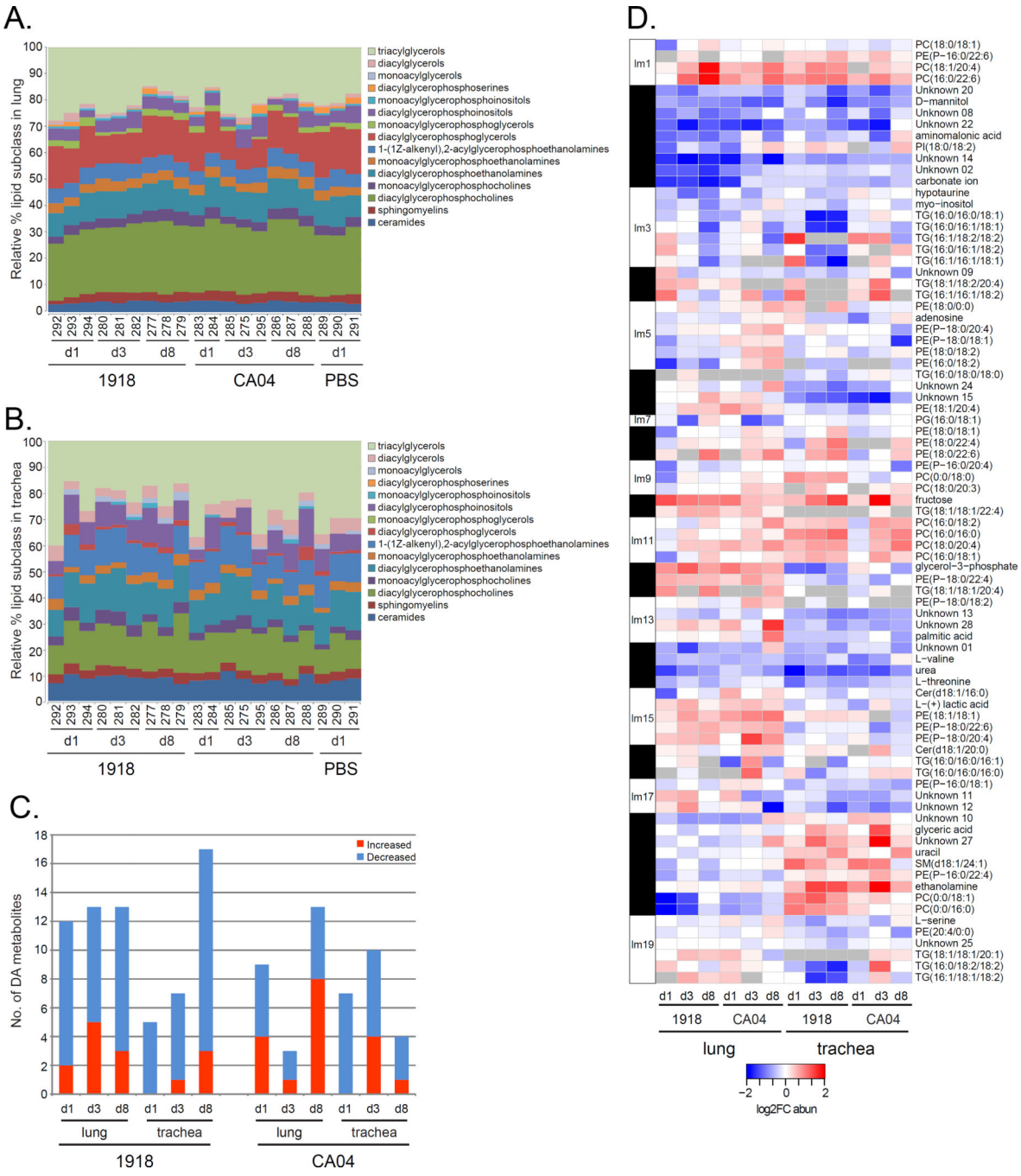

Figure 1. Lipidomic and metabolomic analysis of ferret lung and trachea infected with 1918 and CA04 viruses

A) Lipid subclasses identified in the lung. **B)** Lipid subclasses identified in the trachea. Stacked bar graphs represent the relative percentages of lipid subclasses from individual animals. The lipid subclass annotations are according to the LIPID MAPS structure database (LMSD). **C)** Bar graph showing total number of differentially abundant (DA) metabolites in the lung and trachea of 1918 and CA04 virus-infected ferrets. Comparative statistical analyses of mock with 1918 and CA04 at each time point were performed using a Dunnett

adjusted t-test ($P < 0.05$). Red depicts metabolites with increased abundance relative to mock and blue depicts metabolites with decreased abundance relative to mock. **D)** Heatmap of average log2FC abundances of 50 DA lipids and 33 DA metabolites from the lipid metabolite network inferred for 42 samples corresponding to all time points and both lung and trachea compartments. Modules assignments (1 to 19) are shown on the left-hand side of the heatmap. Missing values in 2 or more replicates were treated as a missing value when averaging the replicates and are depicted as grey. Rows are lipids and metabolites and columns are experimental conditions. See also Table S1 and File S2, first tab.

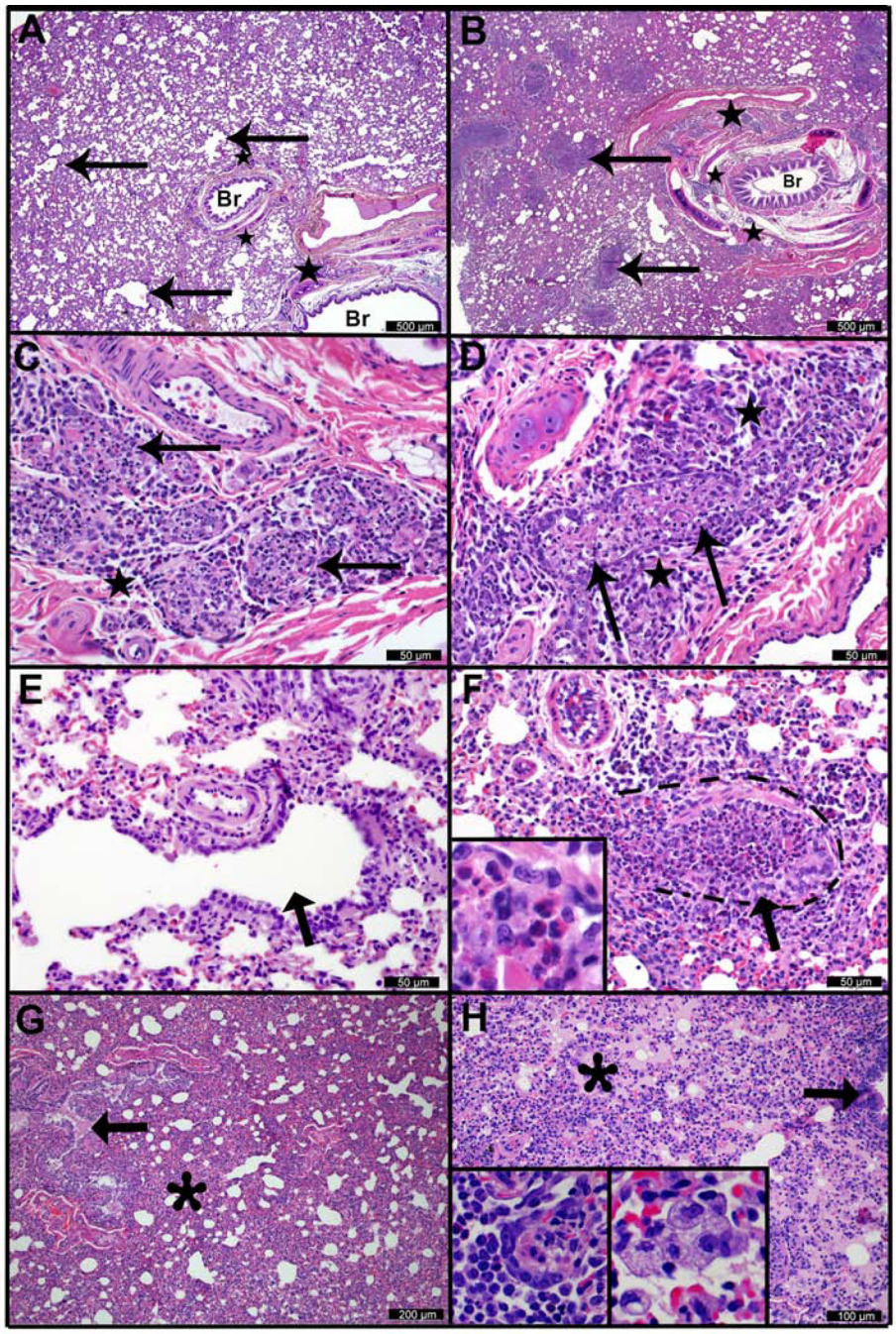

Figure 2. Histologic lesions in ferret lung 3 days after infection with pandemic H1N1 influenza viruses

Histopathological assessment of ferret lung infected with 1918 (left column) or CA04 (right column) viruses. **A)** 1918 virus infection. There is patchy atelectasis and thickening of alveolar walls. “Br” indicates unaffected medium and large bronchioles, and arrows indicate small caliber bronchioles and terminal airways. Stars indicate foci of bronchiolar submucosal gland necrosis and inflammation. **B)** CA04 infection. “Br” indicates large bronchiole containing a crescent of fibrinocellular exudate. Arrows indicate numerous small

caliber bronchioles and terminal airways that have been effaced by necrosis and mixed inflammatory exudates. Adjacent alveolar tissue is consolidated and there is loss of alveolar architectural definition. Stars indicate foci of bronchiolar submucosal gland necrosis and inflammation. **C)** 1918 infection and **D)** CA04 infection. Bronchiolar submucosal gland necrosis. Arrows indicate affected glandular acini in which the epithelium is largely absent and lumena are filled with cellular debris, neutrophils, macrophages and eosinophils. Star indicates periglandular infiltrates of lymphocytes, plasma cells, and eosinophils. **E)** 1918 infection and **F)** CA04 infection. Small bronchioles and terminal airways, higher magnification of micrographs A and B, respectively. Arrows indicate similarly sized transitional and terminal airways. The airway in E is minimally affected. Dashes in F demark the approximate location of the small airway wall. The indicated airway and adjacent alveoli in F exhibit segmental necrosis and ulceration, and the airway lumen is filled with exudate composed of cellular debris and mixed inflammatory cells (**inset F**) including numerous eosinophils, fewer macrophages, lymphocytes and neutrophils. **G)** 1918 infection and **H)** CA04 infection. Regional atelectasis with effusion (asterisks). Arrows indicate bronchioles, the lumen of the bronchiole in G contains effusion (pink material). **H, left inset)** a central C-shaped crescent of Type II pneumocyte hyperplasia and adjacent intra-alvoeolar eosinophils, macrophage, and lymphocytes (left and bottom). **H, right inset)** a cluster of foamy macrophages in an affected alveolus. See also Figure S1.

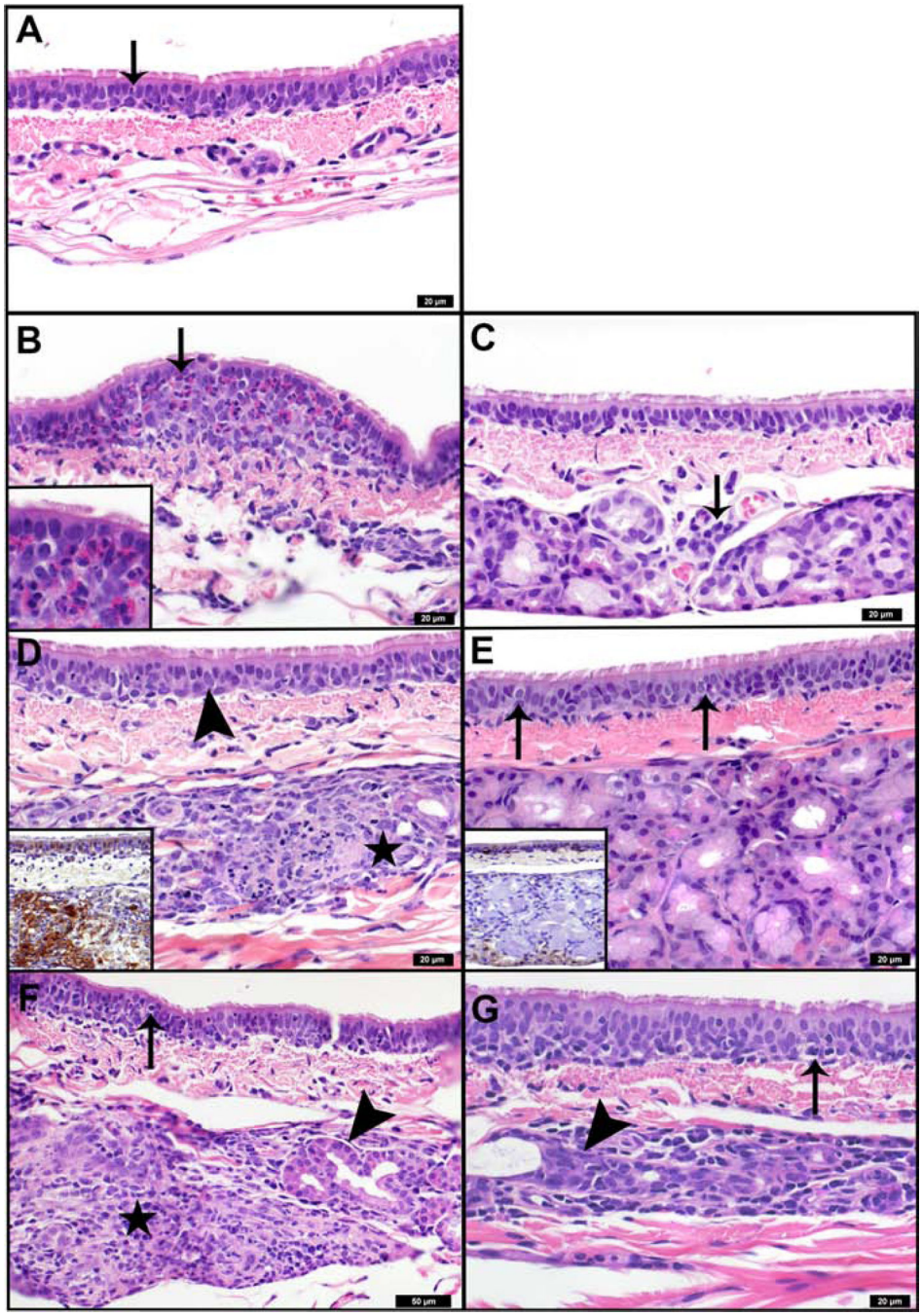

Figure 3. Histologic lesions in ferret trachea infected with pandemic H1N1 influenza viruses, and transcriptomic analysis of host responses

Histopathological assessment of ferret trachea infected with 1918 (left column) or CA04 (right column) viruses. **A)** Mock-infected tracheal mucosa 1 day after infection. Arrow indicates scattered individual eosinophils, and rare neutrophils and lymphocytes within the respiratory epithelium. **B)** Day 1 1918 infection. Arrow indicates nodular expansion of the respiratory epithelium by a predominately eosinophilic infiltrate (inset). Adjacent epithelial cells are disorganized and exhibit moderate variability in cell and nuclear size, and are

occasionally necrotic. **C)** Day 1 CA04 infection. Arrow indicates perivascular aggregate of lymphocytes adjacent to submucosal glands. Scattered lymphocytes are also present in the submucosa and basal regions of the epithelium. There is mild variability in the cell and nuclear size and shape of the respiratory epithelium. **D)** Day 3 1918 infection. Star indicates submucosal gland degeneration and necrosis. Arrow indicates respiratory epithelial cells with cytoplasmic clearing and enlarged irregular nuclei. Affected respiratory and glandular epithelial cells were strongly immunoreactive for polyclonal anti-influenza antibodies (inset, brown staining). **E)** Day 3 CA04 infection. Arrows indicate lymphocytes in respiratory epithelium. Adjacent epithelial cells are mildly disorganized and exhibit mild variability in their cell and nuclear size and shape. Affected respiratory epithelial cells were moderately immunoreactive for polyclonal anti-influenza antibodies (inset, brown staining). Submucosal glands were largely unaffected; however, some reserve cells exhibited positive immunoreactivity. **F)** Day 8 1918 infection and **G)** Day 8 CA04 infection. Remnant submucosal glands are lined by hypertrophic and hyperplastic epithelium (arrowheads). Necrotic glands observed on day 3 (panel D) have been replaced by densely cellular infiltrates of macrophages and lymphocytes (star). Numerous lymphocytes and cellular debris are present in the overlying respiratory epithelium (arrows).

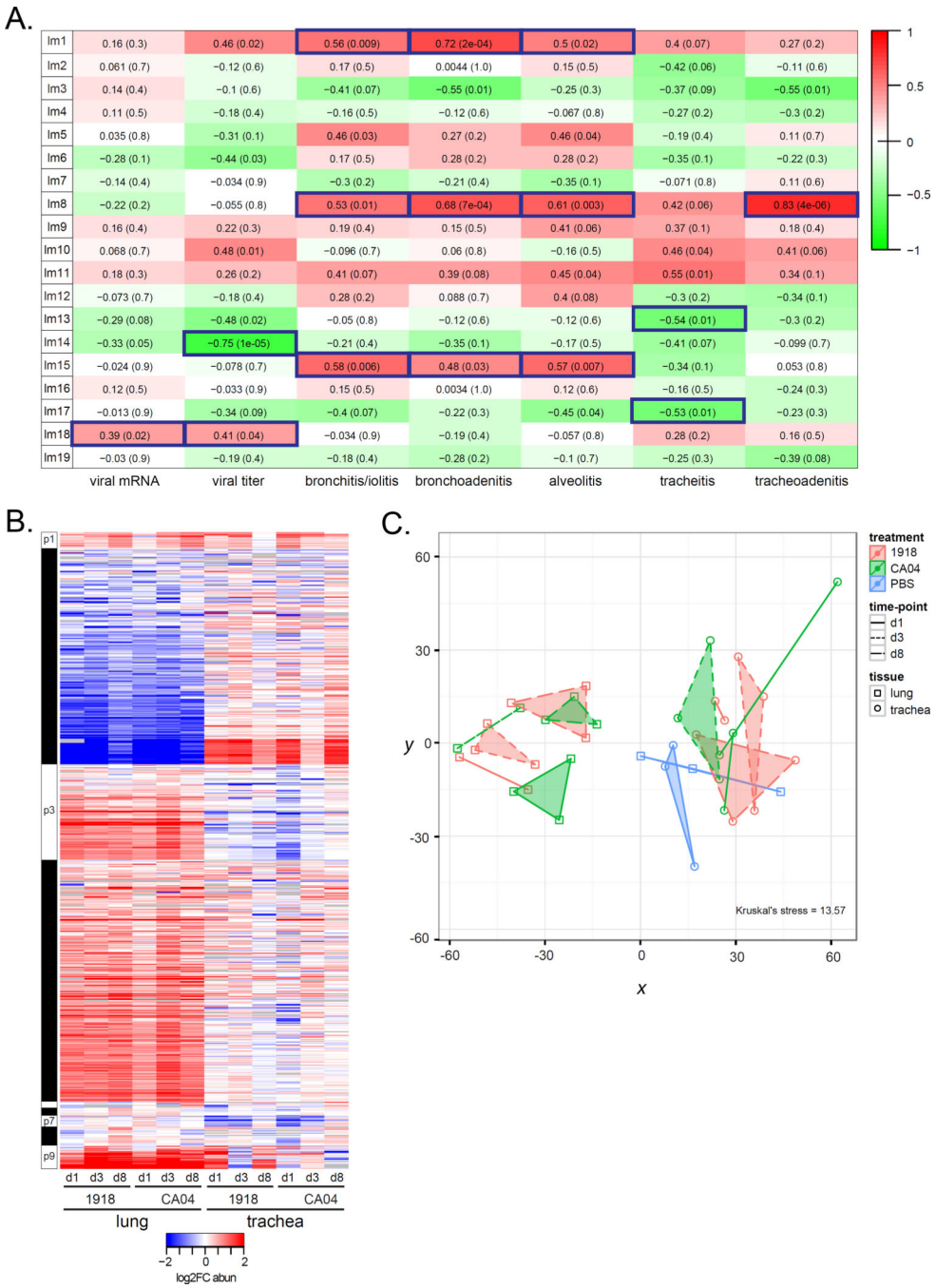

Figure 4. Correlation analysis of lipids and metabolites with phenotypes and protein network analysis

A) Correlation of phenotypic traits (i.e., virologic and histopathologic phenotypes) with lipid metabolite module eigengenes (MEs) using the biweight midcorrelation (bicor) method. Pairwise bicor were calculated between MEs and viral mRNA, viral titer, and histopathologic scores averaged across all subcategories from tracheal, bronchial and alveolar compartments. See also File S1. Listed in each cell of the ME-phenotype matrix is the bicor coefficient and corresponding p-value. Relationships with a $P<0.05$ were considered significant. For example, for the lm1:bronchoadenitis relationship, the bicor

value is 0.72 and the p-value is 2e-04, indicating a significant positive correlation between lm1 and bronchoadenitis. **B)** Heatmap of average log2 FC abundance of 810 DA proteins from the protein network inferred for 37 samples corresponding to all time points and both lung and trachea compartments. Modules assignments (1 to 9) are shown on the left-hand side of the heatmap. Missing values in 2 or more replicates were treated as a missing value when averaging the replicates and are depicted as grey. Rows are proteins and columns are experimental conditions. See also File S2, second tab. **C)** Multidimensional scaling (MDS) representation of the distances among samples based protein log2 abundances (Kruskal's stress = 13.57). The Kruskal stress signifies the amount of information lost due to the dimensionality reduction as a fraction of total information. Points coded as per legend and denote individual animals. Convex hulls link points belonging to the same experimental condition and time point. See also Table S4.

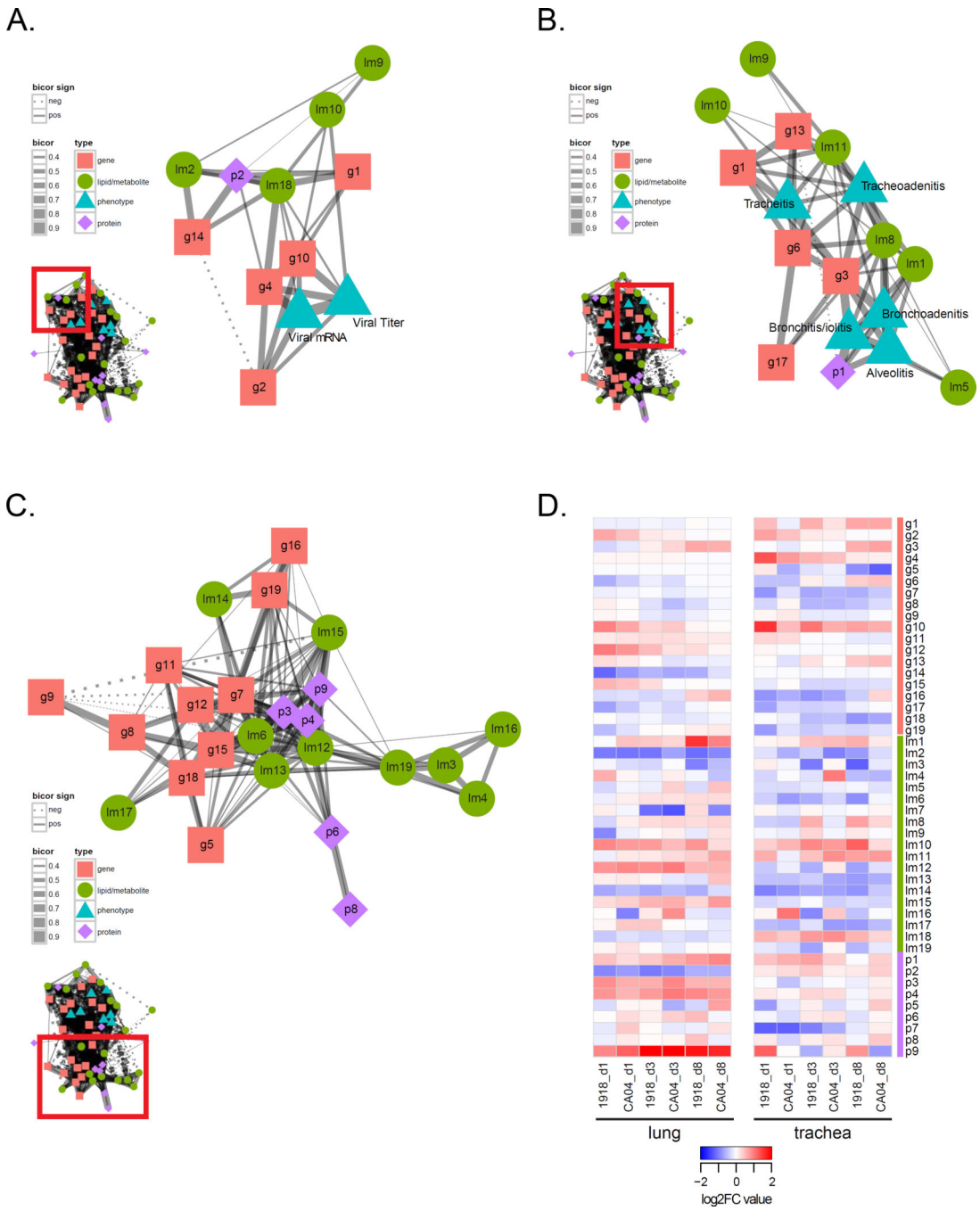

Figure 5. Integrated co-expression network analysis of ferret host responses to pandemic H1N1 influenza virus infection

The integrated omics network related to **A)** influenza virus replication, **B)** respiratory disease, and **C)** relationships among different molecular species. The integrated omics network was constructed by calculating pairwise correlations between modules from independent lipid and metabolite, protein, and gene networks and between all modules and phenotypic data. Nodes represent each module as a single point colored according to data type. Gene (g) modules are symbolized by pink squares. Lipid metabolite (lm) modules are

symbolized by green circles. Protein (p) modules are symbolized by purple diamonds. Phenotype modules are symbolized by blue triangles. Edges between nodes signify biweight midcorrelation (bicor) coefficients between the representative expression profiles (module eigengenes, MEs) of all lipid and metabolite, gene, and protein module pairs with histopathologic and virologic phenotypes. Only significant correlations are shown ($P<0.05$). Positive bicor coefficients are represented by a solid line. Negative bicor coefficients are represented by a dashed line. The line thickness corresponds to the strength of the bicor coefficient (bicor 0.4–0.9). **B)** Dynamics of module expression levels in different respiratory compartments (lung and trachea) and at different time points following infection with either 1918 or CA04 viruses. The heatmap depicts median log2FC values for each module across the experimental dataset. Rows are modules and columns are experimental conditions. See also Figure S3.

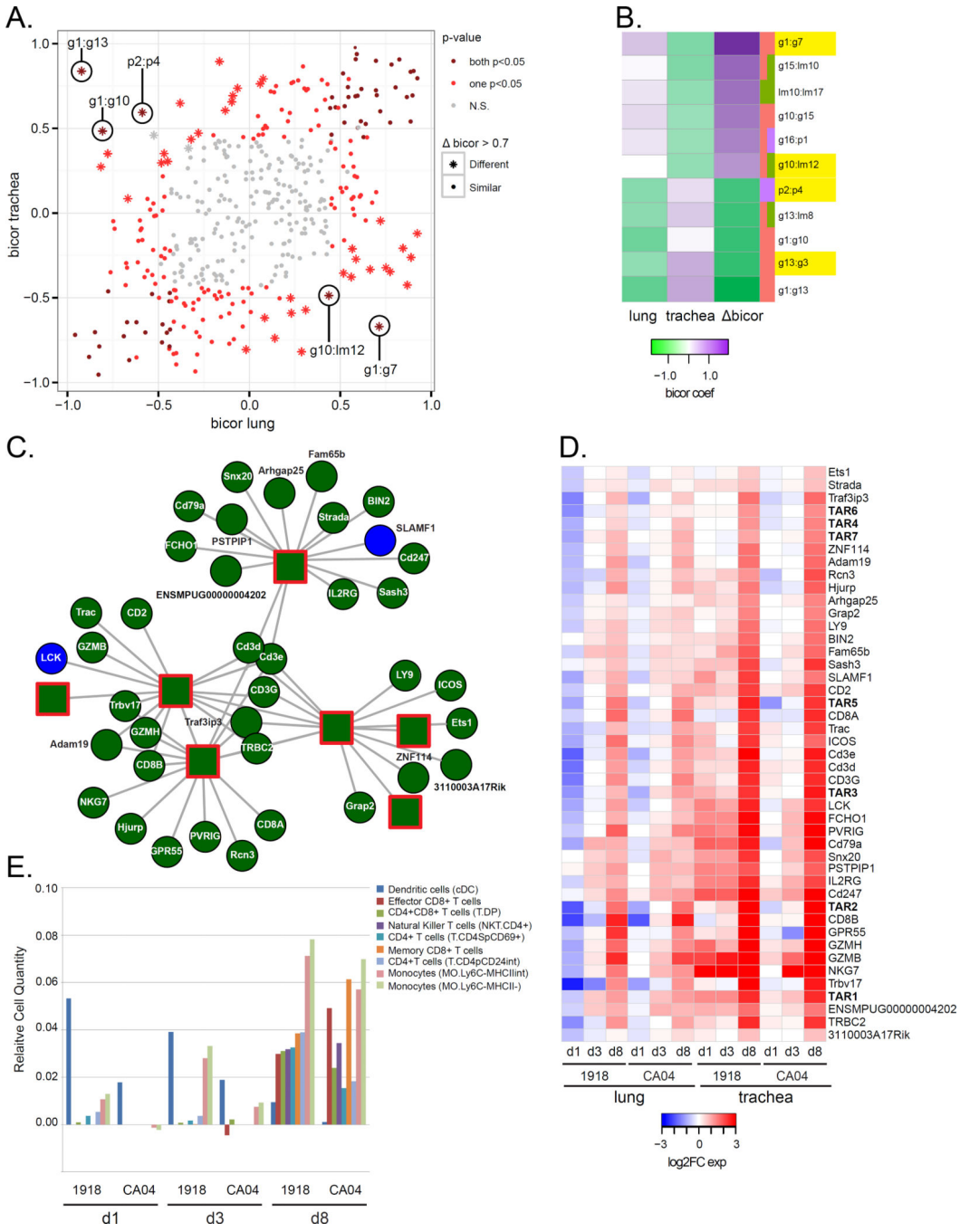

Figure 6. Variation in network information exchange between tissue compartments

For each module of the integrated network, MEs were recalculated considering lung and trachea samples separately. Pairwise correlations between MEs (ME:ME) and between ME and phenotypes (ME:traits) were calculated using the bicor method and separate lung and trachea networks were inferred. **A)** The scatterplot shows the relationships between trachea and lung bicor coefficients. Each point represents an ME:ME comparison and the points are colored according to the p-value of the bicor coefficient. Dark red depicts significant ($p<0.05$) correlations in both lung and trachea networks. Light red depicts significant

($p<0.05$) correlations in either the lung or the trachea network. Grey depicts neither trachea nor lung bicor are significant (N.S.). Star points represent the largest changes in relationships between MEs (absolute Δbicor>0.7). All points in the scatterplot are also represented in the integrated network. **B)** The heatmap shows bicor coefficients in lung and trachea networks for the largest correlation difference between the two tissues. Purple represents positive bicor coefficients and green represents negative bicor coefficients. The difference in correlation between lung and trachea is represented in the column depicting Δbicor values. Edges with an absolute Δbicor value > 0.7 are shown. **C)** Transcriptionally active regions (TARs) hubs, arbitrarily named (i.e., TAR1, TAR2, etc.), from gene module g3 enriched for T cell receptor signaling genes, with the top 15 most correlated entries for each TAR hub shown. Darkgreen nodes = module g3 and blue nodes = module g1. Circles depict coding genes and unannotated genes. Squares with red outline depict TAR hubs. TAR1: tu_XLOC_159227; TAR2: muXLOC_025170; TAR3: mu_XLOC_164742; TAR4: tu_XLOC_232027; TAR5: mu_XLOC_063539; TAR6: mu_XLOC_236016; TAR7: tu_XLOC_232026. **D)** Expression of 45 DE ferret genes and TARs shown in C). The average log2FC values for each virus condition relative to day 1 mock at each time point (days 1, 3 and 8 post-inoculation) in the lung and trachea are shown in the heatmap. Red is increased expression relative to mock and blue is decreased expression relative to mock. White depicts no change in expression. Associated gene names were used for annotation. TARs are in bold. **E)** Predicted immune cell types in the trachea were inferred using Digital Cell Quantifier (DCQ). Cell populations with relative cell quantities > 0.03 in at least 1 of 6 conditions are shown for each virus condition and time-point. The *y*-axis shows the relative cell quantity measure for inferred cells. The *x*-axis shows the inferred cells at each time-point and condition. See also Table S6.

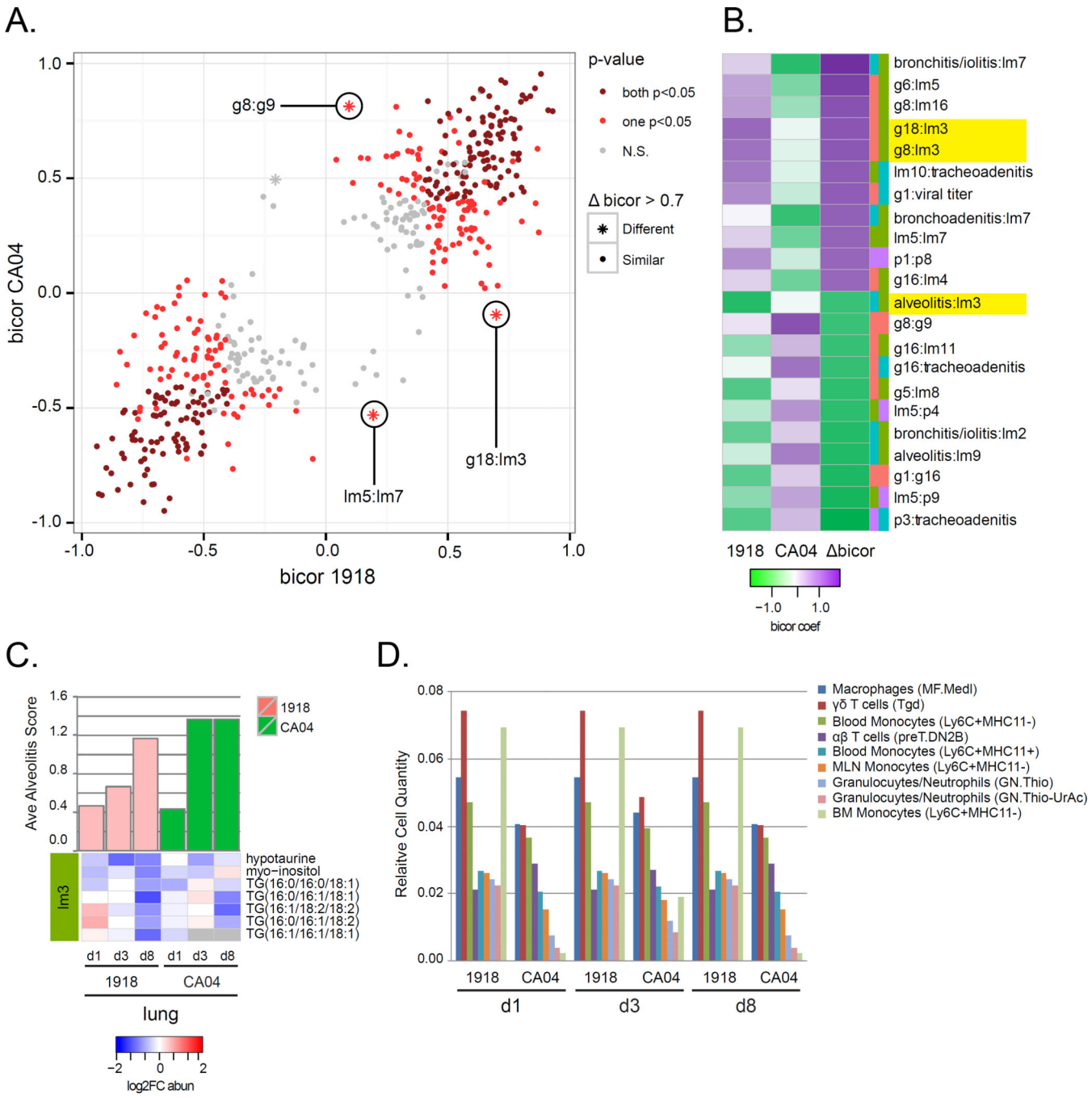

Figure 7. Variation in network information exchange between 1918 and CA04 viruses

For each module of the integrated network, MEs were recalculated considering 1918 and CA04 samples separately. Pairwise correlations between MEs (ME:ME) and between ME and phenotypes (ME:traits) were calculated using the bicor method and separate 1918 and CA04 networks were inferred. **A)** The scatterplot shows the relationships between 1918 and CA04 bicor coefficients. Each point represents an ME:ME comparison and the points are colored according to the p-value of the bicor coefficient. Dark red depicts significant ($p<0.05$) correlations in both 1918 and CA04 networks. Light red depicts significant

($p<0.05$) correlations in either the 1918 or the CA04 network. Grey depicts neither 1918 nor CA04 bicor are significant (N.S.). Star points represent the largest changes in relationships between MEs (absolute Δbicor>0.7). All points in the scatterplot are also represented in the integrated network. **B)** The heatmap shows bicor coefficients in 1918 and CA04 networks for the largest correlation difference between the two viruses. Purple represents positive bicor coefficients and green represents negative bicor coefficients. The difference in correlation between 1918 and CA04 is represented in the column depicting Δbicor values. Edges with an absolute Δbicor value > 0.7 are shown. **C)** Lipid metabolite module lm3 differentially correlated with alveolitis between 1918 and CA04. The ave alveolits score is shown for each condition; 1918 (pink); CA04 (green); PBS (blue). Heatmap of log2FC abundance for lipids and metabolites grouped into lm3 are shown. **D)** Predicted immune cell types in the lung were inferred using DCQ. Cell populations with relative cell quantities > 0.02 in at least 3 of 6 conditions are shown. The *y*-axis shows the relative cell quantity measure for the inferred cells. The *x*-axis shows the inferred cells at each time-point and condition. See also Table S6.